Acta Cryst. (1999). A**55**, 234–245

Decoherence in electron backscattering by kinked dislocations

S. L. Dudarev,* J. Ahmed, P. B. Hirsch and A. J. Wilkinson

Department of Materials, University of Oxford, Parks Road, Oxford OX1 3PH, England.
E-mail: sergei.dudarev@materials.oxford.ac.uk

(*Received 13 October 1998; accepted 10 November 1998*)

Dedicated to Professor A. F. Moodie on the occasion of his 75th birthday†

Abstract

A model is proposed that explains the origin of the bright contrast of dislocation walls consisting of edge dislocation dipoles in electron channelling contrast images (ECCI) of fatigued crystals, when the incident beam is parallel to the edge dislocations. The model is based on the assumption that the contrast arises from the dislocation segments terminating the dipoles. These are modelled as screw-type kinks which scatter electrons. Scattering by randomly distributed kinks leads to the randomization of phase of transmitted and diffracted beams and suppresses the anomalous transmission of electrons. The predicted behaviour of electron-channeling contrast images agrees well with experimental observations.

1. Introduction

Recently, electron-channelling contrast imaging (ECCI) of bulk specimens in a scanning electron microscope (SEM) has emerged as a powerful technique for the study of deformed materials. The technique was first successfully applied by Morin *et al.* (1979) to image dislocations in thin specimens but was not adopted by other groups because it required the use of a specialized SEM with a field-emission gun (FEG) and energy filter. Using optimum specimen geometry conditions and a more efficient detector, Czernuszka *et al.* (1990) showed that individual dislocations could be imaged in a conventional FEG scanning transmission electron microscope (STEM) operating in a SEM mode without the need of an energy filter, and the same has been achieved since in a conventional FEG SEM (Wilkinson & Hirsch, 1995). While the observation of single dislocations by ECCI imposes stringent conditions on the electron optics, these conditions can be relaxed when groups of dislocations are imaged and the technique can be used in conventional SEMs without FEGs (for a review, see Wilkinson & Hirsch, 1997). Using conventional SEMs, ECCI has been used to image groups of interface dislocations in semiconductor heterostructures (Wilkinson *et al.*, 1993), plastic zones around fatigue cracks (Davidson, 1984; Wilkinson *et al.*, 1996), and in particular the dislocation structures in fatigued specimens (Zauter *et al.*, 1992; Schwab *et al.*, 1996; Zhai *et al.*, 1996; Ahmed *et al.*, 1997). The dependence of image contrast on imaging conditions from single or groups of dislocations lying parallel to the specimen surface has been explained in terms of a single forward–backward approximation to multiple scattering (Hirsch & Humphreys, 1970; Wilkinson *et al.*, 1993), taking into account surface relaxation (Wilkinson & Hirsch, 1995). But no attempt has yet been made to explore the contrast from fatigued specimens. The present paper addresses this problem.

Transmission electron microscopy (TEM) studies show that the dislocation structures in single crystals of copper fatigued beyond saturation consist of so-called persistent slip bands (PSBs), which carry most of the plastic strain, separated by a matrix structure consisting of areas of high dislocation density (for a review, see Basinski & Basinski, 1992). Both the matrix and PSBs consist of narrow unfaulted dipoles of edge dislocations of the active primary slip system and of faulted dipoles. TEM studies by Antonopoulos *et al.* (1976) show that the PSBs consist of regularly spaced walls (about 0.15 μm wide) of high density of such dipoles (average dislocation density $\sim 3 \times 10^{15}$ m^{2}), separated by relatively dislocation free channels (dislocation density $\sim 0.2 \times 10^{15}$ m^{2}). This is the so-called ladder structure; the spacing of the walls is typically ~ 1.4 μm. Weak-beam TEM analysis (Antonopoulos *et al.*, 1976) has shown that the typical unfaulted dipole height is ~ 40 Å, while the typical dipole length is ~ 300 Å. The structure also contains a similar density of faulted dipoles, with similar dimensions (for the detailed geometry of the faulted dipoles, see Antonopoulos *et al.*, 1976).

The ECCI images are generally obtained with the electron beam incident either along or at a small angle (up to $\sim 19.5^{\circ}$) to the direction of the edge dislocations constituting the unfaulted dislocation dipoles. With the beam along the direction of the edge dislocations, no contrast should be observable (as in transmission electron microscopy, see Hirsch *et al.*, 1965). The lengths of the faulted dipoles are inclined at about 30 to 35° to the

† With apologies for using two beams instead of three!

ISSN 0108-7673

incident beam, and the stacking faults at about 20°, and some contrast would be expected from the faulted dipoles under these imaging conditions. We believe however that the major contribution to the contrast

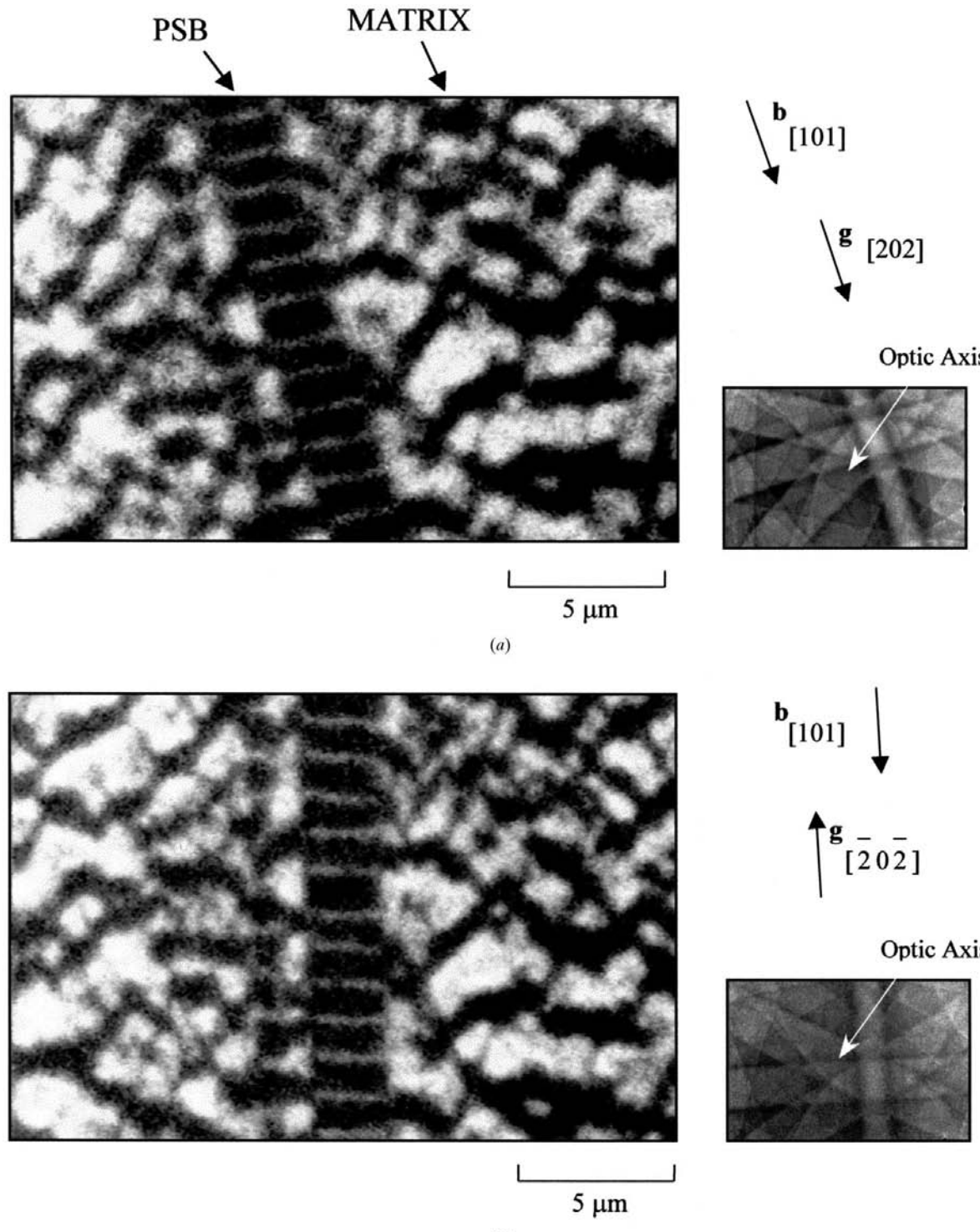

Fig. 1. ECCI micrographs showing dislocation arrangements in a [541] oriented copper single crystal. The crystal was cycled at constant plastic strain amplitude of 2×10^{-3} for $N = 40\,000$ cycles. Note that there is no visible change in the channelling contrast of images obtained for (*a*) $\mathbf{g} \cdot \mathbf{b} = 2$ and (*b*) $\mathbf{g} \cdot \mathbf{b} = -2$. The direction of the incident beam is close to the $[\bar{1}21]$ direction, *i.e.* the direction of the primary edge dislocations.

comes from the short dislocation segments that terminate the dipoles and make very large angles with the incident-beam direction. Such a contrast mechanism is consistent with the experimental facts that the ECCI contrast is independent of incident-beam direction over a range of angles away from the direction parallel to the primary edge dislocation, and is much stronger for the 220-type reflection with **g** parallel to the Burgers vector **b** of the dislocations for which $\mathbf{g}\cdot\mathbf{b}=2$ than with other 220–type reflections with $\mathbf{g}\cdot\mathbf{b}=1$. This paper develops a model for the image contrast from screw-type kinks on edge dislocations parallel to the incident-beam direction, which should describe the main features of the contrast from the segments of mixed character terminating the dislocation dipoles.

The main feature of the approach developed in this paper consists in introducing the idea of randomization of the phase of the wave field of electrons occurring as a result of scattering of electrons by randomly distributed dislocation kinks. In the past, three main types of processes leading to the loss of coherence of the wave field of high-energy electrons were considered: (i) scattering by thermal fluctuations of the potential associated with displacements of atoms from their equilibrium positions in a crystal lattice (Yoshioka, 1957; Howie, 1962; Hall & Hirsch, 1965; Whelan, 1965); (ii) scattering by electronic excitations (Humphreys & Whelan, 1969); (iii) scattering by randomly distributed point defects (Hall *et al.*, 1966; Howie & Stern, 1974; Dudarev *et al.*, 1992). In these three cases, scattering by fluctuations of the interaction potential was treated using perturbative methods, which are valid only if the size of the region where correlations between fluctuations are appreciable is relatively small.

Scattering by randomly displaced dislocation lines cannot be treated using perturbation theory. Since it is not possible to assign a characteristic scale to the elastic field of a dislocation, the distorted-wave Born approximation turns out to be not applicable to the calculation of the amplitude of scattering by fluctuations of the interaction potential associated with kinks on a dislocation line. This means that the treatment of the problem must involve a nonperturbative consideration of scattering of electrons by a dislocation kink followed by the evaluation of the *statistically averaged* cross section of electron backscattering by a crystal containing kinked dislocations. Below, this problem is addressed using the transfer-matrix technique which combines the calculation of electron wave field with the multiple-scattering treatment of electron backscattering. The paper is organized as follows. First, we describe the experimental data. Then, we explain how to treat scattering by dislocation kinks in a nonperturbative way and how to evaluate the statistically averaged cross section of electron backscattering. Finally, we compare the theoretical predictions with experiment.

2. Electron-channelling contrast images of dislocation substructures in fatigued copper single crystals

We start by describing the results of an experimental study of dislocation wall structures observed in fatigued copper single crystals using a scanning electron microscope.

Pure copper single-crystal rods characterized by the [541] surface orientation were kindly provided by Professor Z. S. Basinski and were grown following the procedure described by Basinski & Basinski (1985). The geometry of experimental set-up and the method of specimen preparation followed in our present work are described in a recent paper by Ahmed *et al.* (1997). The specimen geometry and crystallographic orientation were described by Ahmed *et al.* (1998).

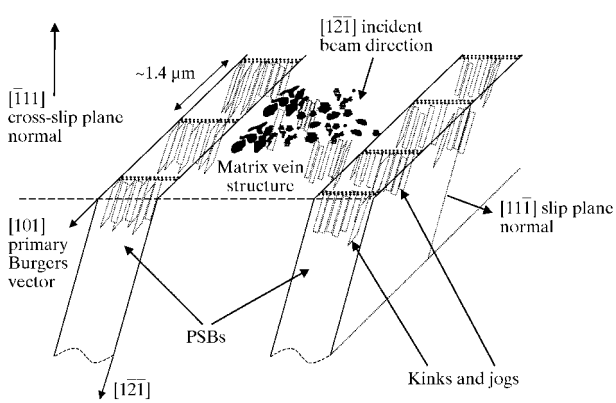

Fig. 2. A diagram showing the geometrical relation between the direction of the incident beam and the dislocation structures shown in Figs. 1(*a*) and (*b*).

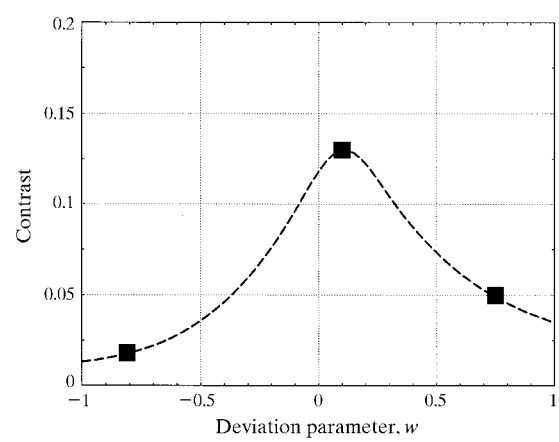

Fig. 3. Contrast *C* of ECCIs (*i.e.* the difference in the level of brightness between the dislocation walls and dark channels in PSB structures) measured experimentally in the SEM as a function of the deviation parameter $w=(\pi^2\hbar^2/m|U_{\mathbf{g}}|)[\mathbf{k}_0^2-(\mathbf{k}_0+\mathbf{g})^2]$ for images with $\mathbf{g}=202$ with the incident-beam direction close to [1$\bar{1}\bar{1}$]. The dashed curve interpolates between experimentally measured values.

The specimens used in experimental observations all had square 4×4 mm cross section and were 60 mm long. These crystals had two special faces, the persistent slip bands (PSB) $(1\bar{2}3)$ faces and the 'cross glide' $(1\bar{1}\bar{1})$ faces; the latter contain the primary Burgers vector $[101]/2$ and thus do not roughen extensively during the test. The primary glide plane is $(11\bar{1})$.

Fatigue tests were carried out at room temperature under plastic strain control using a servo-hydraulic testing machine. The specimens were cyclically deformed in tension compression at a constant plastic shear strain amplitude of 2×10^{-3} measured using a 10 mm clip-on extensometer. Tests were conducted at constant strain rates in the loading and unloading phases using a triangular waveform at the frequency of 1 Hz. Images given in this paper were obtained from a sample tested for 40 000 cycles when the resolved shear stress had saturated at ~28 MPa. The cross glide face was electropolished after fatigue and electron-channelling contrast imaging (ECCI) was subsequently used to observe the dislocation structures in subsurface regions. ECCI images were obtained using a JEOL 6300 microscope at the accelerating voltage of 30 keV (working distance 8 mm, probe current 6×10^{-9} A).

Figs. 1(*a*) and (*b*) are the ECCI micrographs taken from the same area of a $(1\bar{1}\bar{1})$ cross glide face at opposite diffraction conditions $+\mathbf{g}$ and $-\mathbf{g}$, respectively, with the beam incident along the $[1\bar{2}\bar{1}]$ direction, *i.e.* the direction of the primary edge dislocation. The electron channelling patterns (ECPs) shown in Fig. 1 illustrate the diffraction conditions used for ECCI analysis. Fig. 2 illustrates the geometrical relation between the direction of the incident beam and the dislocation structures in the persistent slip bands shown in Figs. 1(*a*) and (*b*). The specimen was aligned to bring the optic axis onto the outer dark region of the selected (202) pseudo-Kikuchi band. The two-beam deviation parameter w ($w = s\xi_{\mathbf{g}}$, as defined in Hirsch *et al.*, 1965) is thus set positive for both micrographs in Fig. 1. The high-dislocation-density regions appear bright in both micrographs. This illustrates a tendency of highly dislocated regions to be brighter than the background irrespective of the diffraction conditions used for ECCI. It is also worth noting that changes in diffraction conditions (from $+\mathbf{g}$ to $-\mathbf{g}$) do not affect the magnitude of ECCI contrast. When the crystal is fatigued in the saturation domain, the dislocations arrange themselves into two distinct phases: the ladder-like persistent slip band structure and the matrix vein structure, both imaged in Fig. 1. Similar contrast is observed for a range of angles of incidence for the same $\mathbf{g}$. Fig. 1 corresponds to $\mathbf{g} \cdot \mathbf{b} = 2$; similar images but with considerably less contrast are obtained with other 220-type reflections for which $\mathbf{g} \cdot \mathbf{b} = 1$.

We performed quantitative measurements of the level of image contrast C between the bright walls and dark channels of the PSB structure. Fig. 3 shows the dependence of contrast C measured experimentally in the SEM for three values of the deviation parameter w for images obtained with $\mathbf{g} = 202$ with the incident beam close to $[1\bar{1}\bar{1}]$ (*i.e.* near to normal incidence). Qualitative observations at other values of w show that the contrast C reaches its maximum value for small positive $w \approx 0.1$ (this corresponds to the darkest part of the channelling band) and slowly decreases away from this condition. The interpolation curve in Fig. 3 describes qualitatively the variation of C with w. Although no measurements of contrast were made with the beam parallel to $[1\bar{2}\bar{1}]$, the variation with w appears to be similar. When the optical axis is set at the brightest part of the channelling pattern (in Fig. 1 this corresponds to the point of intersection of the two main channelling bands), only very low values of contrast C are obtained although micrographs similar to those shown in Fig. 1 with dislocation walls brighter than the surrounding matrix can still be observed.

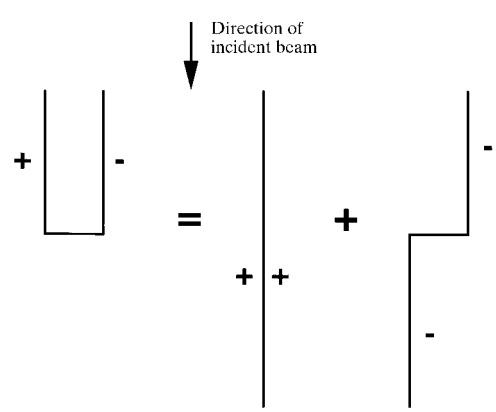

Fig. 4. Schematic drawing illustrating the correspondence between a kink on a dislocation line and a segment terminating a dislocation dipole.

3. Backscattering of electrons by kinked dislocations

In this section, we develop a model illustrating how scattering by randomly distributed kinks on an edge dislocation running nearly parallel to the direction of incidence influences the cross section of electron backscattering. Such a model describes also scattering by screw dislocation segments terminating edge dislocation dipoles, the length of the dipoles being parallel to the incident-beam direction. This can be seen from Fig. 4, which shows that an edge-dislocation dipole viewed end on is equivalent to a kinked edge dislocation plus a straight dislocation of opposite sign, since a straight dislocation viewed end on gives no diffraction contrast.

We start by reviewing the assumptions involved in the treatment of electron backscattering from a defect-free single crystal. In what follows, we consider effects associated with the rapid change of the phase of transmitted and diffracted beams occurring in the vicinity of

kinks. In our model, kinks are treated as sudden sideways displacements of the dislocation line (see below for justification), which is assumed to lie normal to the surface of the crystal. The loss of coherence between transmitted and diffracted beams resulting from random events of scattering by fluctuations of the elastic field associated with kinks leads to the suppression of anomalous transmission of electrons in the vicinity of a kinked dislocation line and to the resulting local increase of backscattering coefficient. Numerical simulation of ECCIs of kinked dislocations shows that the model taking into account scattering of electrons by dislocation kinks can explain the origin of brightening of dislocation walls in the images of fatigued structures.

The mechanism of electron backscattering from a defect-free crystal and the formation of electron-channelling patterns is now well understood (Hirsch & Humphreys, 1970; Dudarev *et al.*, 1995; Dudarev, 1999). The contrast of *energy-unfiltered* electron-channelling patterns can be evaluated on the basis of a solution of the kinetic equation describing a two-stage process involving (i) propagation of incident electrons through the subsurface layer of the crystal, where the coherent superposition of transmitted and diffracted beams gradually fades due to scattering by thermal fluctuation of the crystal potential, and (ii) subsequent multiple scattering of electrons by phonons and electronic excitations, leading to the formation of a broad and relatively featureless distribution of backscattered particles. Diffraction effects occurring at the first stage are responsible for a noticeable (~10%) variation of the total coefficient of electron backscattering observed as a function of the orientation of the beam of incident electrons with respect to the atomic planes. The coefficient of backscattering is minimum for the directions of incidence corresponding to larger than average depth of penetration of electrons into the crystal. The increase in the average penetration depth for certain directions of incidence is associated with diffraction effects leading to the preferential population of weakly absorbed Bloch waves. For the directions of incidence where electrons populate Bloch states characterized by higher than average absorption coefficients, the cross section of electron backscattering is larger than the average background value (Booker *et al.*, 1967; Joy *et al.*, 1982).

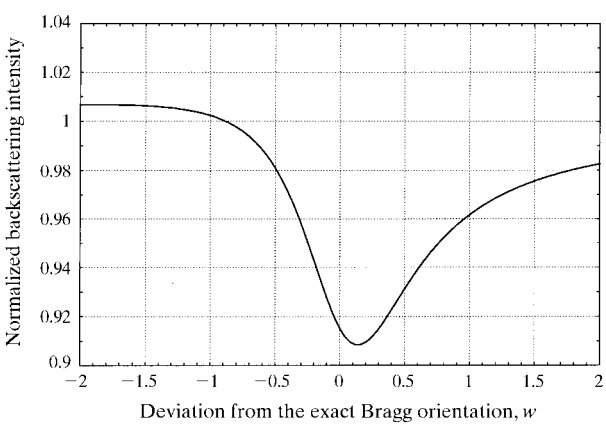

Fig. 5. The profile $R(w)$ of the copper (220) electron-channelling band calculated using equation (1) and assuming that the energy of the incident electrons is $E = 30$ keV. Values of the Fourier components of the potential U_0, $U_{\mathbf{g}}$ and $U_{-\mathbf{g}}$ used in the calculation were taken from Radi (1970). The deviation parameter w is defined as $w = -\varepsilon/2|U_{\mathbf{g}}| = (\pi^2\hbar^2/m|U_{\mathbf{g}}|)[\mathbf{k}_0^2 - (\mathbf{k}_0 + \mathbf{g})^2]$, where $\mathbf{k}_0$ is the wavevector of incident electrons.

In an explicit form, the dependence of the total cross section of electron backscattering R on the angle of incidence is given by the following expression, which can be obtained using a perturbation expansion of a solution of the kinetic equation for the density matrix obtained by Dudarev *et al.* (1995):

$$R = R_{\mathrm{bg}} - \mathcal{K} \int_0^\infty z \sum_{l,h} \varphi_l^*(\mathbf{r}) U''_{lh}(\mathbf{r}) \varphi_h(\mathbf{r})\, \mathrm{d}z. \qquad (1)$$

In this equation, R_{bg} is the coefficient of backscattering averaged over a range of directions of incidence and $\mathcal{K}$ is a constant factor that depends on the geometry of scattering and on the position and the sensitivity of the detector of backscattered electrons. Equation (1) represents the first two terms of the Taylor expansion of the solution of the kinetic equation describing backscattering of electrons from a crystal in terms of the ratio $l_{\mathrm{imfp}}/l_{\mathrm{tr}}$ of the inelastic mean free path l_{imfp} to the transport length l_{tr} [see Section V of the paper by Dudarev *et al.* (1995) for more details]. The integration in (1) is performed along a straight line parallel to the incident beam and z denotes the projection of $\mathbf{r}$ on the inner normal to the surface. The quantity $U''_{lh}(\mathbf{r})$ represents the phonon imaginary part of the potential [the dependence of the Fourier components of the potential $U_{lh}(\mathbf{r})$ on $\mathbf{r}$ results from the presence of elastic displacement field $\mathbf{u}(\mathbf{r})$] and $\varphi_h(\mathbf{r})$ and $\varphi_l^*(\mathbf{r})$ are the amplitudes of diffracted ($h, l \neq 0$) and transmitted ($h, l = 0$) beams. These amplitudes are defined assuming that the expression for a plane wave describing an electron with wavevector $\mathbf{k}_0$ is $\exp(2\pi i \mathbf{k}_0 \cdot \mathbf{r})$. Amplitudes $\varphi_h(\mathbf{r})$ satisfy the system of dynamical equations

$$\begin{aligned} i(2\pi\hbar^2/m)(\mathbf{k}_0 + \mathbf{g})\partial\varphi_h(\mathbf{r})/\partial\mathbf{r} \\ = (2\pi^2\hbar^2/m)[(\mathbf{k}_0 + \mathbf{g})^2 - \mathbf{k}_0^2]\varphi_h(\mathbf{r}) \\ + \sum_t \left[U'_{ht}(\mathbf{r}) - iU''_{ht}(\mathbf{r})\right]\varphi_t(\mathbf{r}), \end{aligned} \qquad (2)$$

where the Fourier components of the potential depend on the displacement field $\mathbf{u}(\mathbf{r})$ *via*

$$U_{ht}(\mathbf{r}) = U_{hl} \exp[-2\pi i(\mathbf{g}_h - \mathbf{g}_l) \cdot \mathbf{u}(\mathbf{r})]. \qquad (3)$$

In some cases, it is convenient to make a gauge transformation of equations (2) and transfer the dependence on the local displacement field $\mathbf{u}(\mathbf{r})$ from the Fourier

components of the potential to the amplitudes. By defining

$$\Phi_h(\mathbf{r}) = \varphi_h(\mathbf{r}) \exp[2\pi i \mathbf{g}_h \cdot \mathbf{u}(\mathbf{r})], \tag{4}$$

we arrive at the system of Howie–Whelan equations

$$\begin{aligned} i(2\pi\hbar^2/m)(\mathbf{k}_0 + \mathbf{g})\partial\Phi_h(\mathbf{r})/\partial\mathbf{r} \\ = -\Phi_h(\mathbf{r})\frac{2\pi\hbar^2}{m}\left\{(\mathbf{k}_0 + \mathbf{g}) \cdot \frac{\partial}{\partial\mathbf{r}}\right\} 2\pi[\mathbf{g}_h \cdot \mathbf{u}(\mathbf{r})] \\ + (2\pi^2\hbar^2/m)[(\mathbf{k}_0 + \mathbf{g})^2 - \mathbf{k}_0^2]\Phi_h(\mathbf{r}) \\ + \sum_t (U'_{ht} - iU''_{ht})\Phi_t(\mathbf{r}). \end{aligned} \tag{5}$$

The Fourier components of the potential entering the Howie–Whelan equations are independent of $\mathbf{r}$ even in the presence of an inhomogeneous field of elastic displacements $\mathbf{u}(\mathbf{r})$. The price paid for this simplification consists in the appearance of a new term in the right-hand side of equations (5). This new term is proportional to the derivative of $\mathbf{u}(\mathbf{r})$ and accounts for the local change in the angle between the atomic planes and the wavevector of electrons propagating in the crystal. If the scalar product $\mathbf{g}_h \cdot \mathbf{u}(\mathbf{r})$ remains constant along the path followed by the incident electrons, the derivative in the right-hand side of (5) vanishes and the coefficient of backscattering turns out to be independent of the coordinate of the point where the incident beam enters the crystal (that is why dislocation lines running parallel to the incident beam cannot be seen in ECCIs). It is also evident that any discontinuity of the displacement field occurring along the path of the incident beam will lead to the appearance of a δ-function term in the right-hand side of the Howie–Whelan equations.

In principle, elastic displacement fields associated with dislocations are continuous functions of $\mathbf{r}$ (with the exception of points situated on dislocation lines themselves) and therefore the chance of finding a δ-function term in the Howie–Whelan equations is purely hypothetical. However, if the characteristic scale of variation of the displacement field in the direction of the incident beam is small (*i.e.* where this scale is substantially smaller than the scale of variation of wave functions describing dynamical diffraction of electrons), the behaviour of the first term in the right-hand side of (5) may look similar to a narrow δ-function peak. In this case, it is simpler to deal with an artificial discontinuous displacement field and with the associated δ-function term rather than with real continuous (but rapidly varying) functions $\mathbf{g}_h \cdot \mathbf{u}(\mathbf{r})$. In this paper, we consider a model that may serve as an illustration of the latter case.

As mentioned above, to explain why the dislocation walls *are* indeed seen in ECCI images, we analyse a model where we assume that dislocation walls are formed by edge dislocations parallel to the incident-beam direction with short screw segments normal to this direction, representing either kinks or segments termi-

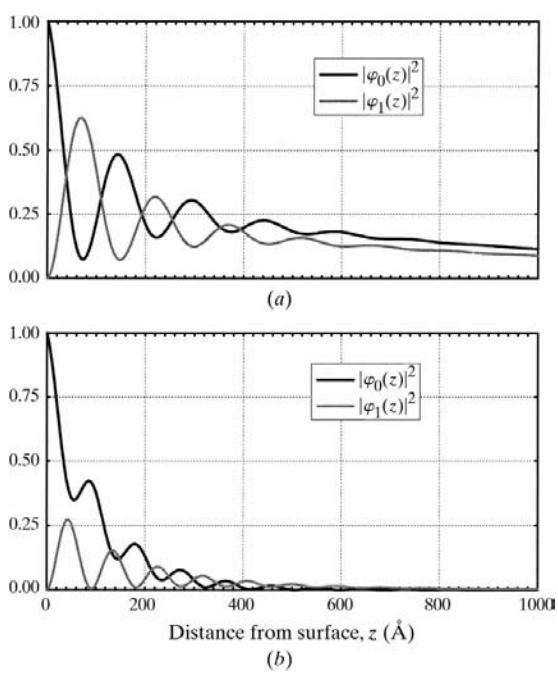

Fig. 6. Intensities $|\varphi_0(z)|^2$ and $|\varphi_{\mathbf{g}}(z)|^2$ of the transmitted and diffracted beams evaluated for the case of diffraction of 30 keV electrons in a copper single crystal for (*a*) $w = 0.14$ ($\varepsilon = -2$ eV), where the intensity of backscattering is minimum, (*b*) $w = -1.4$ ($\varepsilon = 20$ eV), corresponding to the maximum of the function $R(w)$ shown in Fig. 5.

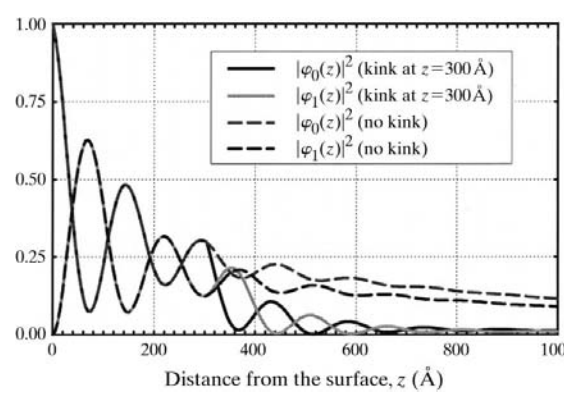

Fig. 7. Intensities $|\varphi_0(z)|^2$ and $|\varphi_{\mathbf{g}}(z)|^2$ of the transmitted and diffracted beams calculated as a function of the depth z of penetration of electrons in a copper single crystal for $w = 0.14$ [the minimum of the function $R(w)$]. Dashed curves coincide with those shown in Fig. 6(*a*). Solid curves represent intensities of the transmitted and diffracted beams calculated for a crystal with a kink on a dislocation line. The kink corresponds to a sudden displacement of the dislocation line occurring at $z = 300$ Å. The vector of the displacement $\mathbf{h} = (0.5, 0.0, 0.0)$ (in dimensionless units) is assumed to be parallel to the surface of the crystal. Between $z = 0$ and $z = 300$ Å, the position of the dislocation line coincides with the z axis. The beam of electrons enters the crystal at the point $x = 0.01$ and $y = 0.01$.

nating edge dislocation dipoles. Yoffe (1960*a*,*b*) has derived the displacement around a kinked dislocation. In order to simplify the computations, we have assumed that a typical kink height, h, is small compared with the extinction distance ξ_g. As shown in Appendix A, if terms of order h/ξ_g are neglected, the displacement field around a kinked dislocation then approximates to a superposition of elastic strain fields from segments of straight dislocations shifted as a whole in the (x, y) plane at the kink position. This approximation is appropriate for the structure of dipole walls in fatigued crystals of copper, for which the typical dipole height has been found to be ~40 Å, (Antonopoulos *et al.*, 1976), compared with the extinction distance for $\mathbf{g} = 202$ at 30 kV, $\xi_g \sim 250$ Å.

This approximation results in a discontinuity in displacement at the kink. To avoid dealing with δ-function terms entering the Howie–Whelan equations, we evaluate the cross section of electron backscattering (1) by solving dynamical equations (2) where the dependence of the Fourier components of the potential on atomic displacements is retained in the phase factor (3). Before proceeding further, we note that the system of equations (2) possesses an interesting property that simplifies the numerical evaluation of the contrast of channelling images. Using (2) and evaluating the gradient of the sum of intensities of diffracted beams $\sum_h |\varphi_h(\mathbf{r})|^2$, we arrive at

$$\frac{2\pi\hbar^2}{m}\frac{\partial}{\partial \mathbf{r}}\sum_h (\mathbf{k}_0 + \mathbf{g}_h)|\varphi_h(\mathbf{r})|^2 = -\sum_{l,h} \varphi_h^*(\mathbf{r})U''_{hl}(\mathbf{r})\varphi_l(\mathbf{r}). \tag{6}$$

In the case where the imaginary part $U''_{hl}(\mathbf{r})$ of the crystal potential vanishes, equation (6) becomes equivalent to the condition of conservation of current.

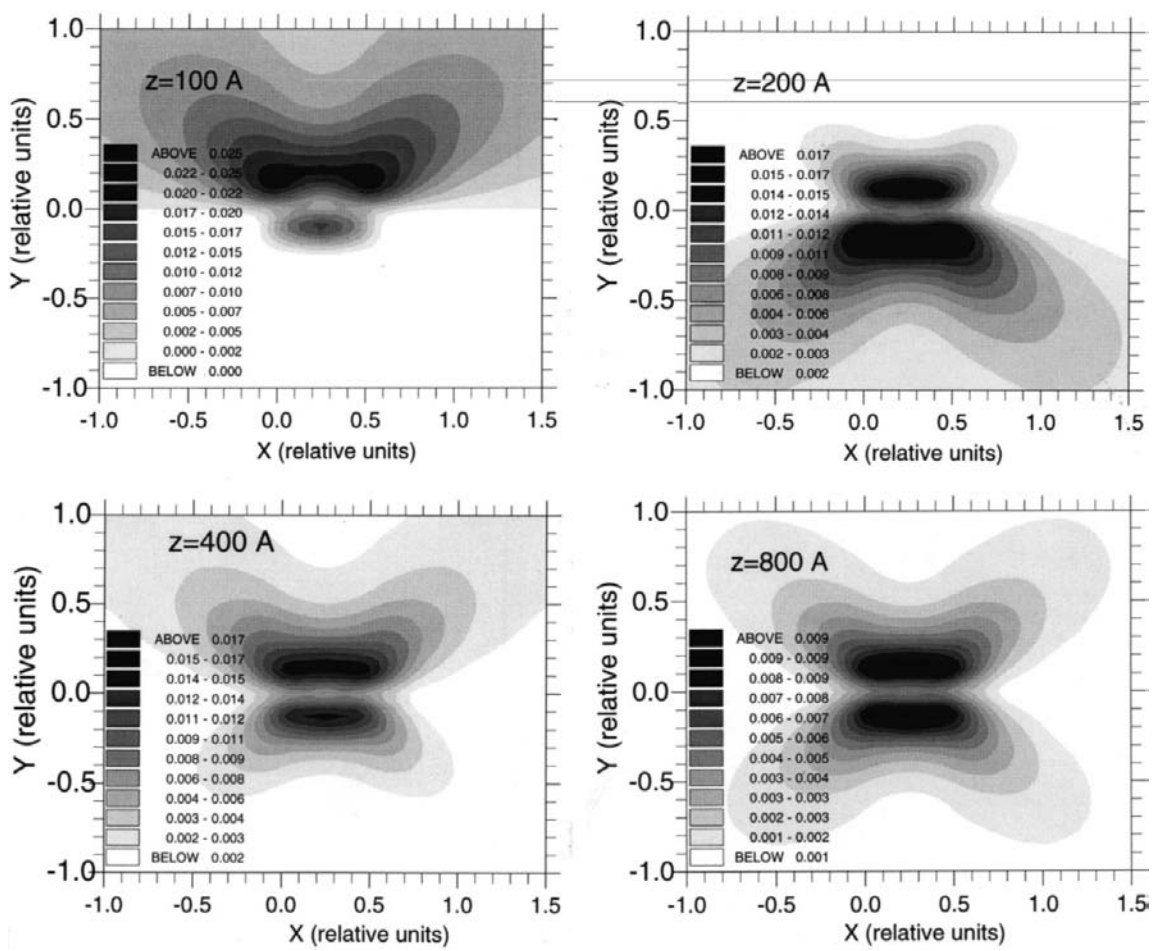

Fig. 8. Dependence of ECCIs of a dislocation kink on the distance between the kink and the surface. The values of z shown in simulated images correspond to the distance from the entrance surface where the core of the dislocation is displaced by $\mathbf{h} = (0.5, 0.0, 0.0)$ in dimensionless units [note the lack of scale in the definition of the polar angle in equation (11)]. The grey scale is chosen in such a way that regions corresponding to the highest level of backscattering intensity are shown as black. Note that in experimental images the high-intensity regions are brighter than the background.

For electrons incident along z, normal to the surface, we neglect the x and y components of the gradient operator [this amounts to neglecting $\mathbf{g}_h$ in (6) and replacing $\mathbf{k}_0 \cdot \nabla$ by $k_0 \partial/\partial z$] and after the integration of (1) by parts obtain

$$R = R_{\mathrm{bg}} - \mathcal{K}(2\pi\hbar^2 k_0/m) \int_0^\infty \mathrm{d}z \sum_h |\varphi_h(\mathbf{r})|^2. \qquad (7)$$

In the two-beam case, only two amplitudes need to be retained in (7). In this case, the coefficient of back-scattering is given by:

$$R = R_{\mathrm{bg}} - \mathcal{K}(2\pi\hbar^2 k_0/m) \int_0^\infty \mathrm{d}z \left[|\varphi_0(\mathbf{r})|^2 + |\varphi_{\mathbf{g}}(\mathbf{r})|^2\right]. \quad (8)$$

To evaluate the amplitudes $\varphi_0(\mathbf{r})$ and $\varphi_{\mathbf{g}}(\mathbf{r})$ of the transmitted and diffracted beams of electrons propagating in a distorted crystal, we need to solve a system of two coupled differential equations

$$\begin{aligned} i\frac{\partial}{\partial t}\varphi_0(x,y,t) &= U_0\varphi_0(x,y,t) \\ &\quad + U_{-\mathbf{g}} \exp[2\pi i \mathbf{g}\cdot\mathbf{u}(x,y,t)]\varphi_{\mathbf{g}}(x,y,t) \\ i\frac{\partial}{\partial t}\varphi_{\mathbf{g}}(x,y,t) &= (\varepsilon + U_0)\varphi_{\mathbf{g}}(x,y,t) \\ &\quad + U_{\mathbf{g}} \exp[-2\pi i \mathbf{g}\cdot\mathbf{u}(x,y,t)]\varphi_0(x,y,t), \end{aligned} \qquad (9)$$

complemented with boundary conditions $\varphi_0(x,y,0) = 1$ and $\varphi_{\mathbf{g}}(x,y,0) = 0$. In equations (9), $t = mz/2\pi\hbar^2 k_0$, U_0 and $U_{\pm\mathbf{g}}$ are the Fourier components of the potential [values of U_0 and $U_{\pm\mathbf{g}}$ used in the calculations were taken from tables by Radi (1970)]. Parameter ε, which determines the deviation of the direction of incidence from the exact Bragg orientation and which is given by $\varepsilon = (2\pi^2\hbar^2/m)[(\mathbf{k}_0 + \mathbf{g})^2 - \mathbf{k}_0^2]$, is related to a more familiar quantity w *via* $w = -\varepsilon/2|U_{\mathbf{g}}|$.

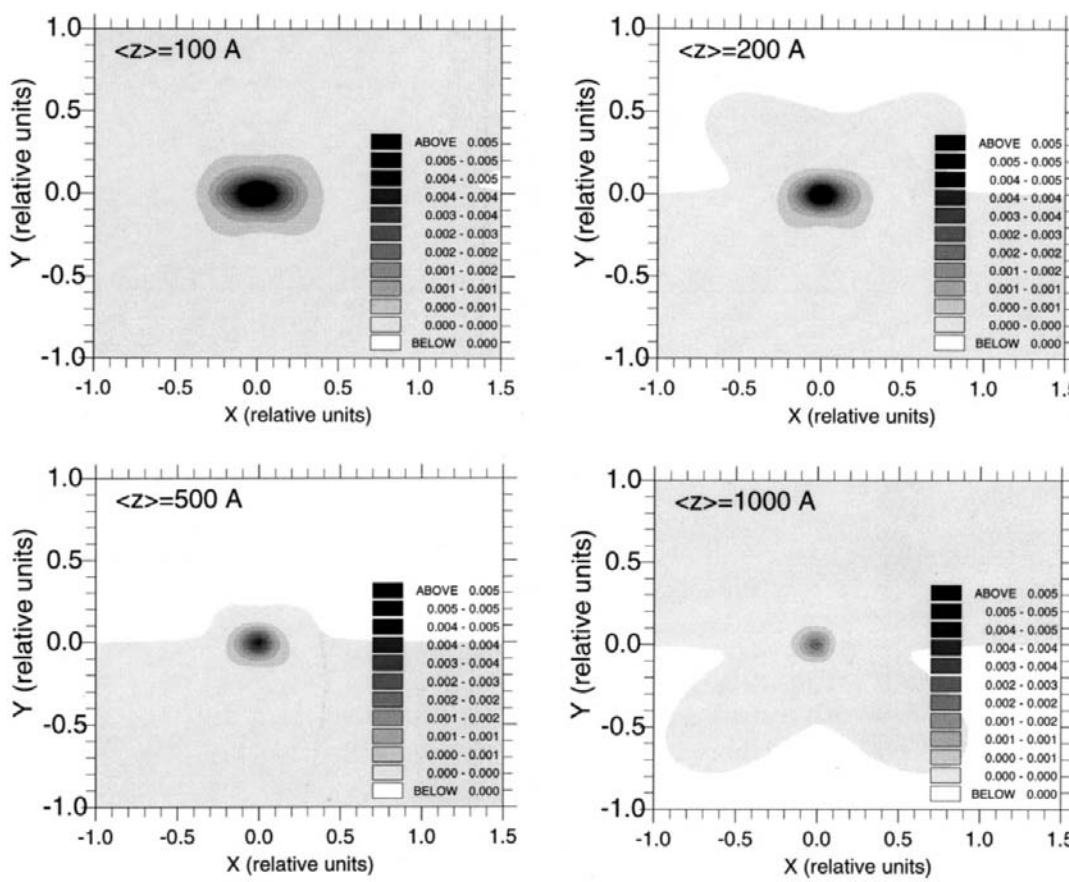

Fig. 9. ECCIs of kinked dislocations simulated using the Monte Carlo approach. $\langle z \rangle$ denotes the average distance between kinks on the dislocation line. Positive and negative displacements $\mathbf{h} = (\pm 0.5, 0.0, 0.0)$ (in dimensionless units) of the dislocation line are assumed to occur with equal probabilities.

In the case where the reciprocal-lattice vector $\mathbf{g}$ is parallel to the x axis, only the x component of the field of elastic displacements of an edge dislocation needs to be considered:

$$u_x(\mathbf{r}) = \frac{b}{2\pi}\left[\Theta + \frac{1}{4(1-\nu)}\sin(2\Theta)\right], \qquad (10)$$

where ν is the Poisson coefficient and the Burgers vector $\mathbf{b}$ of the dislocation is assumed to be parallel to the x axis. Θ denotes the polar angle

$$\Theta = \begin{cases} \arccos\left(\dfrac{x-x_0}{[(x-x_0)^2+(y-y_0)^2]^{1/2}}\right), \\ \qquad\qquad \text{when } y - y_0 > 0 \\ 2\pi - \arccos\left(\dfrac{x-x_0}{[(x-x_0)^2+(y-y_0)^2]^{1/2}}\right), \\ \qquad\qquad \text{when } y - y_0 < 0. \end{cases} \qquad (11)$$

In this equation, x_0 and y_0 are the coordinates of the centre of the dislocation. To compare ECCIs simulated using (1) and (9) with experimental ECCIs of dislocation walls discussed in the previous section, we assume that $\mathbf{b} = \frac{1}{2}(101)$ and $\mathbf{g} = 202$, *i.e.* $\mathbf{g}\cdot\mathbf{b} = 2$. The phase factor $\exp[2\pi i\mathbf{g}\cdot\mathbf{u}(x,y,t)]$ is given by

$$\exp[2\pi i\mathbf{g}\cdot\mathbf{u}(x,y,t)] = \exp\left\{2i\left[\Theta + \frac{\sin(2\Theta)}{4(1-\sigma)}\right]\right\}.$$

Numerical integration of (9) was carried out using the transfer-matrix technique. The transfer matrix $\hat{T}(x,y,t,\Delta t)$ relates the amplitudes of transmitted and diffracted beams at the entrance and exit surfaces of a thin slab Δt parallel to the surface of the crystal:

$$\begin{bmatrix} \varphi_0(x,y,t+\Delta t) \\ \varphi_{\mathbf{g}}(x,y,t+\Delta t) \end{bmatrix} = \exp[iU_0\Delta t - i(\varepsilon/2)\Delta t] \times \begin{bmatrix} T_{00}(x,y,t,\Delta t), & T_{0\mathbf{g}}(x,y,t,\Delta t) \\ T_{\mathbf{g}0}(x,y,t,\Delta t), & T_{\mathbf{gg}}(x,y,t,\Delta t) \end{bmatrix} \times \begin{bmatrix} \varphi_0(x,y,t) \\ \varphi_{\mathbf{g}}(x,y,t) \end{bmatrix}, \qquad (12)$$

where

$$\begin{aligned} T_{00}(x,y,t,\Delta t) &= \cos\left[\Delta t(U_{\mathbf{g}}U_{-\mathbf{g}} + \varepsilon^2/4)^{1/2}\right] + i\frac{\varepsilon/2}{(U_{\mathbf{g}}U_{-\mathbf{g}} + \varepsilon^2/4)^{1/2}} \times \sin\left[\Delta t(U_{\mathbf{g}}U_{-\mathbf{g}} + \varepsilon^2/4)^{1/2}\right] \\ T_{0\mathbf{g}}(x,y,t,\Delta t) &= -i\frac{U_{-\mathbf{g}}\exp[2\pi i\mathbf{g}\cdot\mathbf{u}(x,y,t)]}{(U_{\mathbf{g}}U_{-\mathbf{g}} + \varepsilon^2/4)^{1/2}} \times \sin\left[\Delta t(U_{\mathbf{g}}U_{-\mathbf{g}} + \varepsilon^2/4)^{1/2}\right] \\ T_{\mathbf{g}0}(x,y,t,\Delta t) &= -i\frac{U_{\mathbf{g}}\exp[-2\pi i\mathbf{g}\cdot\mathbf{u}(x,y,t)]}{(U_{\mathbf{g}}U_{-\mathbf{g}} + \varepsilon^2/4)^{1/2}} \times \sin\left[\Delta t U_{\mathbf{g}}U_{-\mathbf{g}} + \varepsilon^2/4)^{1/2}\right] \\ T_{\mathbf{gg}}(x,y,t,\Delta t) &= \cos\left[\Delta t(U_{\mathbf{g}}U_{-\mathbf{g}} + \varepsilon^2/4)^{1/2}\right] - i\frac{\varepsilon/2}{(U_{\mathbf{g}}U_{-\mathbf{g}} + \varepsilon^2/4)^{1/2}} \times \sin\left[\Delta t(U_{\mathbf{g}}U_{-\mathbf{g}} + \varepsilon^2/4)^{1/2}\right]. \end{aligned} \qquad (13)$$

A product of transfer matrices evaluated for a set of slices gives the transfer matrix for a finite layer. By multiplying transfer matrices, it is possible to find amplitudes of the transmitted and diffracted beams at any given distance from the entrance surface. This *does not* require evaluating the derivative of the displacement field $\mathbf{u}(x,y,t)$ and therefore the transfer-matrix approach turns out to be suitable for solving equations (9) even in the case where $\mathbf{u}(x,y,t)$ is a rapidly varying or even a discontinuous function of t.

We start by evaluating the dependence of the coefficient of electron backscattering (8) on the angle of incidence (R depends on the angle of incidence *via* a dimensionless parameter $w = -\varepsilon/2|U_{\mathbf{g}}|$, which characterizes the deviation of the direction of incidence from the Bragg orientation). A profile of the copper (202) electron-channelling band calculated using (8) is shown in Fig. 5. The minimum of backscattering intensity at $w \approx 0.14$ is associated with the anomalously deep penetration of electrons in the crystal occurring at the respective angle of incidence. The appearance of the maximum of the curve shown in Fig. 5 at $w \approx -2$ is due to anomalous absorption of electrons. To illustrate the difference in the behaviour of the wave field of electrons in the crystal occurring in the two cases $w \approx 0.14$ and $w \approx -2$, in Fig. 6 we plot intensities $|\varphi_0(z)|^2$ and $|\varphi_{\mathbf{g}}(z)|^2$ of the transmitted and diffracted beams calculated as a function of the distance z from the surface of the crystal. In the case (*a*) corresponding to the minimum of backscattering intensity, the wave function of electrons attenuates very slowly into the crystal bulk while in the case (*b*) the intensity of diffracted beams decreases very rapidly due to enhanced scattering by thermal fluctuations of the potential.

Scattering by dislocation kinks has a profound effect on the wave field of electrons propagating in the crystal. Fig. 7 shows the dependence of the intensity of trans-

mitted and diffracted beams calculated for two cases: for a perfect crystal and for a crystal containing a dislocation, the core of which is suddenly displaced in the x direction in the plane $z = 300$ Å. Results shown in Fig. 7 indicate that the discontinuity of the crystal potential occurring in the vicinity of the kink leads to a substantial increase in the rate of phonon scattering of electrons in the region $z > 300$ Å.

To understand in more detail how sudden displacements of dislocation lines influence electron backscattering and ECCIs of fatigued crystals, we analysed the dependence of ECCI images of dislocation kinks on the distance between the surface and the kink. Fig. 8 shows a series of simulated ECCIs of dislocation kinks. All the images were simulated for $w = 0.14$ (this value of w corresponds to the minimum of the curve shown in Fig. 5). The dependence of image contrast on z follows a pattern correlated with the spatial structure of the wave field of incident electrons shown in Fig. 7. The contrast of the image oscillates (retaining its sign in the central part of the image) as a function of z for $z \leq 600$ Å. The presence of these oscillations of image contrast are associated with oscillations of the wave field of incident electrons shown in Fig. 7. For $z \geq 600$ Å, oscillations of the wave field vanish and the ECCI contrast becomes a monotonic function of z. The area of particularly high intensity seen in the centre of the image is associated with a very rapid variation of the crystal potential in the vicinity of the kink [in simulations we assumed that the core of the dislocation gets displaced from $(x_0, y_0) = (0, 0)$ to $(x_0, y_0) = (0.5, 0)$ (in relative units) at the respective value of z].

The contrast of ECCIs shown in Fig. 8 depends both on the *direction* of the displacement of the dislocation core and also on the distance between the kink and the surface. In a real crystal, a dislocation line may wander in both x and y directions (*i.e.* kinks along x and jogs along y) and the average distance between kinks or jogs may vary depending on the microscopic structure of the dislocation walls. To analyse the influence of these two factors on image contrast, we carried out computer simulations of images of dislocations with *randomly* distributed screw-type *kinks of either sign*. Again, we assumed that the direction of incidence corresponds to the minimum of the channelling band profile shown in Fig. 5. Results of statistical Monte Carlo simulations of ECCI images of dislocations characterized by four different values of the *average line density* of kinks are shown in Fig. 9. The Monte Carlo algorithm used for simulating dislocation lines was based on the assumption that a line may be displaced in both the positive and negative directions of x axis and that these displacements were equally probable. We assumed that the average distance between the kinks $\langle z \rangle$ was the only parameter that characterized the scale of kinks in the dislocation lines. Examination of images in Fig. 9 shows that scattering by randomly distributed kinks gives rise to the overall increase of the cross section of electron backscattering for the regions that are close to the dislocation core. This result does not depend on the sign of the $\mathbf{g}$ vector used for imaging since any dependence on the sign vanishes after statistical averaging over displacements of the dislocation line. Fig. 9 exhibits a noticeable although relatively weak oscillatory dependence of image contrast on $\langle z \rangle$. This is a dimensional effect occurring when the average distance between kinks becomes comparable with the period of oscillations of the wave field of electrons (see Fig. 7). There also exists a noticeable correlation between the average distance between the kinks and the degree of enhancement of the cross section of backscattering. The higher the volume density of kinks, the stronger is the effect.

Similar computations were carried out for the case $\mathbf{g} \cdot \mathbf{b} = 1$. While the maximum brightness is comparable to the case for $\mathbf{g} \cdot \mathbf{b} = 2$, the width of the image is much greater for $\mathbf{g} \cdot \mathbf{b} = 2$. The experimentally observed contrast arises from dipoles distributed over the wall width (0.15 μm) and this will correlate with the integrated brightness over the individual images. This is much greater for $\mathbf{g} \cdot \mathbf{b} = 2$ than for $\mathbf{g} \cdot \mathbf{b} = 1$, in agreement with experiment.

The computer simulations of ECCI of kinked dislocations (Figs. 8 and 9) show that if the angle of incidence of electrons is chosen in such a way that the penetration depth of the wave field of electrons is large (*i.e.* if the angle of incidence corresponds to the minimum of intensity on the channelling band profile) then scattering by a kinked dislocation leads to the increase in the coefficient of backscattering. This agrees with the experimental images shown in Fig. 1 where dislocation walls appear brighter than the background or, in other words, where the local coefficient of electron backscattering turns out to be larger for regions characterized by higher density of dislocations. We also analysed how the contrast of a simulated image of a kink depends on the parameter w characterizing the deviation of the angle of incidence from the exact Bragg condition. We defined the contrast as the difference in the intensity between the brightest (or darkest) point in the image and the average backscattering coefficient corresponding to the same value of w. The value of $\mathcal{K}$ was chosen to match the scale of experimental curve shown in Fig. 3. The dependence of image contrast on w is shown in Fig. 10. The curve shown in Fig. 10 shows remarkable similarity to the experimental curve of Fig. 3. Slight oscillations of the curve shown in Fig. 10 result from a dimensional effect (calculations were performed assuming that the kink was buried 500 Å below the surface). The contrast becomes negative in the region of large negative values of w. However, the possibility of observing the contrast reversal experimentally is impeded by the very small magnitude of contrast in that region (the level of contrast is approximately ten times lower than its peak value corresponding to the vicinity

of $w \approx 0$). No calculations were carried out for the many beam conditions corresponding to the brightest part of the channelling pattern, at which very weak but bright dislocation wall images were observed (see §2).

4. Conclusions

In this paper, we describe a relatively simple model that explains the origin of the bright contrast of dislocation walls seen in electron channelling contrast images of fatigued crystals. The model explains: (i) the experimentally observed lack of dependence of the contrast of fatigued structures on the sign of the reciprocal-lattice vector **g** used for diffraction imaging; (ii) the fact that the image contrast for $\mathbf{g} \cdot \mathbf{b} = 2$ is greater than that for $\mathbf{g} \cdot \mathbf{b} = 1$; (iii) the fact that the dislocation walls appear bright for a range of positive and negative values of w; and (iv) the variation of contrast with w. The model involves the assumption that dislocation lines running nearly parallel to the incident beam have kinks, which scatter electrons, and that scattering by randomly distributed kinks leads to the randomization of phase of transmitted and diffracted beams. We formulated an efficient algorithm for the Monte Carlo simulation of images of dislocations with kinks of either sign and showed that image simulations may help in clarifying the origin of experimentally observed phenomena. Although no calculations have been carried out, we expect that jogs and kinks with mixed character on edge dislocations will have similar effects.

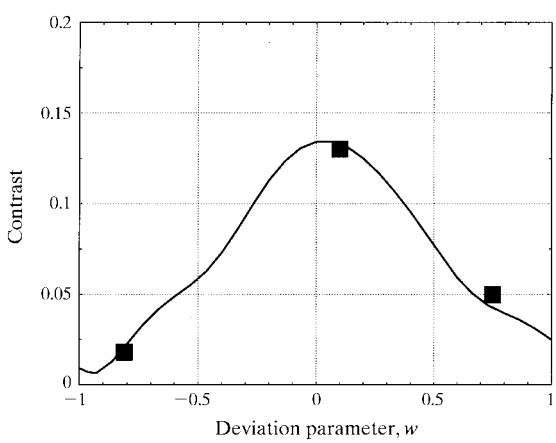

Fig. 10. The contrast of a simulated image of a dislocation kink buried 500 Å below the surface of the crystal plotted as a function of the deviation parameter w. Weak oscillations seen in the image result from oscillations of the wave field of electrons. For large negative values of w, the function shown in this figure changes its sign but the magnitude of the image contrast remains many times smaller than its peak value corresponding to $w \approx 0.05$. Squares represent experimental points taken from Fig. 3.

APPENDIX *A*

In this Appendix, we evaluate the x component of the displacement field around a kink on an edge dislocation. The purpose of this derivation is to estimate the range of validity of the 'sudden displacement approximation' adopted for the description of a kinked dislocation earlier in the paper. Using the Yoffe (1960*a*,*b*) formula for the displacement field of an angular dislocation [where we take into account corrections noted by Shaibani & Hazzledine (1981)] and assuming that both **b** and **g** are parallel to the x axis [the latter means that only the $u_x(x, y, z)$ component entering the product $\mathbf{u}(\mathbf{r}) \cdot \mathbf{g}$ needs to be retained], we obtain

$$
\begin{aligned}
u_x(x, y, z) &= (b/4\pi)(y/|y|)\Bigg(\pi/2 - \arctan(x/|y|) \\
&\quad + [(z - z_0)/|z - z_0|] \\
&\quad \times \arctan\left\{\frac{x|z - z_0|}{|y|[x^2 + y^2 + (z - z_0)^2]^{1/2}}\right\}\Bigg) \\
&\quad + (b/4\pi)(y/|y|)\Bigg((\pi/2) + \arctan[(h - x)/|y|] \\
&\quad + [(z - z_0)/|z - z_0|] \\
&\quad \times \arctan\left\{\frac{(h - x)|z - z_0|}{|y|[(h - x)^2 + y^2 + (z - z_0)^2]^{1/2}}\right\}\Bigg) \\
&\quad + [b/8\pi(1 - \nu)]\Bigg\{[xy/(x^2 + y^2)] \\
&\quad - \frac{xy(z - z_0)}{(x^2 + y^2)[x^2 + y^2 + (z - z_0)^2]^{1/2}} \\
&\quad + \{(x - h)y/[(x - h)^2 + y^2]\} \\
&\quad + \frac{(x - h)y(z - z_0)}{[(x - h)^2 + y^2][(x - h)^2 + y^2 + (z - z_0)^2]^{1/2}}\Bigg\}.
\end{aligned}
\tag{14}
$$

The same result can be obtained directly from Burgers' formula (Hirth & Lothe, 1982):

$$
\mathbf{u}(\mathbf{r}) = -\frac{\mathbf{b}}{4\pi}\iint \frac{\mathbf{R} \cdot \mathrm{d}\mathbf{A}'}{R^3} - \frac{1}{4\pi}\int \frac{\mathbf{b} \times \mathrm{d}\mathbf{l}'}{R} + \frac{1}{8\pi(1 - \nu)}\frac{\partial}{\partial \mathbf{r}}\int \frac{(\mathbf{b} \times \mathbf{R}) \cdot \mathrm{d}\mathbf{l}'}{R},
$$

where $\mathrm{d}\mathbf{A}' = \mathrm{d}x'\mathrm{d}z'\mathbf{n}$, the unit normal vector $\mathbf{n}$ is given by $(0, -1, 0)$ and $\mathbf{R} = \mathbf{r}' - \mathbf{r} = (x' - x, -y, z' - z)$.

In the limiting case $h = 0$, expression (14) coincides with the known formula for the x component of the displacement field of an infinite straight-edge dislocation (Landau & Lifshits, 1970). This equation shows that for a given size h of the kink on a dislocation line the

characteristic scale of variation of $u_x(x, y, z)$ as a function of z is also given by h (this is of course not surprising since h is the only dimensional parameter entering the problem). Since the typical size of a kink on a dislocation line is of the order of magnitude of 40 Å, we conclude that the characteristic scale of variation of $u_x(x, y, z)$ as a function of z is typically much smaller than the extinction distance $\xi_g \sim \hbar^2 k_0/m|U_{\mathbf{g}}| \sim 250$ Å. Neglecting the terms of the order of $h/\xi_g \ll 1$, we arrive at the model where the field of displacements around a kinked dislocation is represented by a superposition of elastic fields of segments of straight dislocations shifted as a whole in the (x, y) plane.

Computer simulations were performed in the Materials Modelling Laboratory of the Department of Materials at the University of Oxford. Our thanks are due to Professor B. Cantor for provision of facilities, and BNFL (SLD), the Royal Society (AJW) and EPSRC (JA) for financial support.

References

Ahmed, J., Wilkinson, A. J. & Roberts, S. G. (1997). *Philos. Mag. Lett.* **76**, 237–245.

Ahmed, J., Wilkinson, A. J. & Roberts, S. G. (1998). EBSD Workshop, Oxford, April 1998. *J. Microsc.* Submitted.

Antonopoulos, J. G., Brown, L. M. & Winter, A. T. (1976). *Philos. Mag.* **34**, 549–557.

Basinski, Z. S. & Basinski, S. J. (1985). *Acta Metal.* **33**, 1307–1317.

Basinski, Z. S. & Basinski, S. J. (1992). *Prog. Mater. Sci.* pp. 89–148.

Booker, G. R., Shaw, A. M. B., Whelan, M. J. & Hirsch, P. B. (1967). *Philos. Mag.* **16**, 1185–1191.

Czernuszka, J. T., Long, N. J., Boyes, E. D. & Hirsch, P. B. (1990). *Philos. Mag. Lett.* **62**, 227–232.

Davidson, D. L. (1984). *Int. Met. Rev.* **29**, 75–97.

Dudarev, S. L. (1999). In *Topics in Electron Diffraction and Microscopy of Materials*, edited by P. B. Hirsch. Bristol: Institute of Physics.

Dudarev, S. L., Peng, L.-M. & Whelan, M. J. (1992). *Surf Sci.* **279**, 380–394.

Dudarev, S. L., Rez, P. & Whelan, M. J. (1995). *Phys. Rev. B*, **51**, 3397–3412.

Hall, C. R. & Hirsch, P. B. (1965). *Proc. R. Soc. London Ser. A*, **286**, 158–172.

Hall, C. R., Hirsch, P. B. & Booker, G. R. (1966). *Philos. Mag.* **14**, 979–989.

Hirsch, P. B., Howie, A., Nicholson, R., Pashley, D. W. & Whelan, M. J. (1965) *Electron Microscopy of Thin Crystals.* London: Butterworth.

Hirsch, P. B. & Humphreys, C. J. (1970) *Scanning Electron Microscopy 1970*, edited by O. Johari, pp. 451–455. Chicago: IIT Research Institute.

Hirth, J. P. & Lothe, J. (1982). *Theory of Dislocations*, 2nd ed., p. 102. New York: Wiley.

Howie, A. (1962). *Proc. 5th International Congress on Electron Microscopy, Philadelphia*, papers AA9, AA10. New York: Academic Press.

Howie, A. & Stern, R. M. (1974). *Z. Naturforsch. Teil A*, **27**, 382–389.

Humphreys, C. J. & Whelan, M. J. (1969). *Philos. Mag.* **20**, 165–172.

Joy, D. C., Newbury, D. E. & Davidson, D. L. (1982). *J. Appl. Phys.* **53**, R81–R122.

Landau, L. D. & Lifshits, E. M. (1970). *Theory of Elasticity*, Section 27. Oxford: Pergamon.

Morin, P., Pitaval, M., Besnard, D. & Fontaine, G. (1979). *Philos. Mag.* **50**, 511–519.

Radi, G. (1970). *Acta Cryst.* A**26**, 41–56.

Schwab, A., Bretschneider, J., Buque, C., Blochwitz, C. & Holste, C. (1996). *Philos. Mag. Lett.* **74**, 449–454.

Shaibani, S. J. & Hazzledine, P. M. (1981). *Philos. Mag.* **44**, 657–665.

Whelan, M. J. (1965). *J. Appl. Phys.* **36**, 2099–2103, 2103–2110.

Wilkinson, A. J., Anstis, G. R., Czernuszka, J. T., Long, N. J. & Hirsch, P. B. (1993). *Philos. Mag.* A**68**, 59–80.

Wilkinson, A. J., Henderson, M. B. & Martin, J. W. (1996). *Philos. Mag. Lett.* **74**, 145–151.

Wilkinson, A. J. & Hirsch, P. B. (1995). *Philos. Mag.* A**72**, 81–103.

Wilkinson, A. J. & Hirsch, P. B. (1997). *Micron*, **28**, 279–308.

Yoffe, E. H. (1960*a*). *Philos. Mag.* **5**, 161–169.

Yoffe, E. H. (1960*b*). *Philos. Mag.* **6**, 1147–1155.

Yoshioka, H. (1957). *J. Phys. Soc. Jpn*, **12**, 618–628.

Zauter, R., Petry, F., Bayerlein, M., Sommer, C., Christ, H.-J. & Mughrabi, H. (1992), *Philos. Mag.* A**66**, 425–436.

Zhai, T., Martin, J. W., Briggs, G. A. D. & Wilkinson, A. J. (1996). *Acta Mater.* **44**, 3477–3488.